

A study of the effect of Ti-Al-V microalloying on the mechanical and physical properties of invar 36



Mehmet Kul^a, Bekir Akgül^{b,*}, Yusuf Ziya Karabay^c, Kaan Pehlivanoglu^c, Bahadir Türkyaman^c⁷

^a Department of Metallurgical and Materials Engineering, Sivas University of Science and Technology, Sivas 58000, Turkey

^b Department of Aeronautical Engineering, Sivas University of Science and Technology, Sivas 58000, Turkey

^c TÜBİTAK SAGE, Advanced Materials Technologies Division, PK 16, Mamak, Ankara, Turkey

ARTICLE INFO

4

Keywords:
Invar 36
Microalloying
Low CTE
High Mechanical Properties
Electromagnetic interference (EMI) shielding

ABSTRACT

In this study, the effect of the addition of the Ti-Al-V triple refiner to invar 36 on the mechanical and physical properties was studied in detail. In addition, the shielding of electromagnetic interference (EMI) performance was investigated in range of X-band (8 – 12 GHz). The maximum hardness and tensile strength of the refiner-treated sample were obtained 195 HV₅ and 611 MPa, respectively, while the average grain size was reduced from 100 µm to 40 µm. Mechanical features such as hardness and tensile strength were improved with the Ti-Al-V triple refiner and hot forging processes due to grain boundary strengthening. The minimum coefficient of thermal expansion (CTE) was $1.14 \times 10^{-6}/^{\circ}\text{C}$ at 20 – 100 °C for the hot-forged plain invar alloy. The grain/twin boundaries and residual stresses formed after forging inhibit lattice vibrations, which are naturally responsible for thermal expansion of solids. The EMI shielding performance of invar 36 was analyzed in range of ~55 to ~65 dB for the 1 mm thick sheet through 8 – 12 GHz.

1. Introduction

Invar 36, which was discovered by Guillaume in 1897 [1], is often preferred in applications where the thermal expansion coefficient is desired very low, especially in the aerospace, defense, and electronic industries. For example, it is widely used in composite tooling moulds, accelerometers, hermetic packaging, and various optical components for glass-to-metal sealing. However, invar 36 is ductile due to its single austenite phase; therefore, its application area is limited. As is known for austenitic steels, austenite in structures becomes more stable as the stacking fault energy increases, depending on the increasing Ni ratio [2]. Since invar 36 can be classified among materials with medium stacking fault energy (~122 mJ/m²), it is not hardened by quenching treatment [3]. In particular, the high Ni and low carbon content (< 0.005 wt%), which stabilizes austenite, complicates the martensitic transformation of invar 36 [4]. In general, stress-induced martensitic transformation (SIMT) occurs in austenitic stainless steel. The SIMT process is not complete in invar 36 because the thermodynamic T-zero temperature is lower than that of other austenitic stainless steels. SIMT could be realized under cryogenic deformation conditions for invar 36.

For these reasons, many researchers have conducted various studies focusing on other hardening methods instead of quenching hardening.

Methods such as solid solution strengthening [5], fine crystal strengthening [6–10], working hardening [11–14] and precipitation hardening [15–18] have been studied extensively in the literature. However, among these methods, the fine crystal strengthening is the most effective method because it is easy to apply and low in cost. It is known that when the grain size in the microstructure is reduced, the grain boundary intensity increases dramatically [4,19,20]. These grain boundaries considerably contribute to the strength improvement of metallic materials by hindering dislocation motion. The same dislocations can facilitate the plastic deformation by easily moving within the crystal and interacting with each other [21]. During plastic deformation, while dislocations move readily in certain planes and orientations within the grain, these motions are hindered by randomly located atoms at the grain boundary and result in dislocation aggregation. As a result of this, the mechanical properties of materials such as hardness and tensile strength are improved by dislocation agglomeration and high-energy grain boundaries. This strengthening phenomenon is known as grain boundary strengthening and is based on the Hall-Petch mechanism, which is related to grain size [22]. Increasing grain boundaries is the most effective way of preventing dislocation movement without disturbing the CTE. Even though various plastic deformation processes are applied to decrease grain size, as a result of these, excessive dislocation

* Corresponding author.

E-mail address: bekirakgul@sivas.edu.tr (B. Akgül).

4

and residual stress accumulation are formed in the structure, which is an undesired state [11,12,23]. These excessive residual stresses have a detrimental effect on the dimensional stability of invar 36 in service [2]. For example, while the CTE of Invar 36 was $0.7 \times 10^{-6} / ^\circ\text{C}$ when subjected to severe plastic deformation (SPD), the CTE increased abruptly to $2.4 \times 10^{-6} / ^\circ\text{C}$ after heat treatment at 350°C in the study by Bitkulov et al. [11]. This is due to residual stresses in the structure formed by SPD, which inhibit lattice vibrations responsible for thermal expansion.

However, the addition of various alloying elements in trace amounts to invar 36 as grain refiners can effectively reduce the grain size without causing excessive residual stress and dislocation density. In general, grain refiners activate the heterogeneous nucleation mechanism by forming chemically high melting point intermetallic phases and/or MC-type carbides with elements which present in the molten metal [2,6,7,15,24,25]. These numerous particles play an effective role as heterogeneous nucleation centres, refining the crystals without further growth through the solidification process. Various alloying elements such as Zr, Ce, La, Ti and Nb are known to be used as grain refiners in the invar 36 alloy [6–9]. Among them, Ti and Nb have a strong carbide forming properties [9]. MC-type compounds formed by reactions between Ti or Nb and sufficient amounts of C additionally contribute to heterogeneous nucleation. However, it should be noted that these types of compounds can accumulate at grain boundaries, and this phenomenon can result in a weakening of the material strength. For instance, in the Hong-Guang et al. study, Ce-La added as a double refiner caused catastrophic damage by creating a brittle phase (Fe-Ni-Ce-La) along the grain boundaries in the invar alloy [6]. Therefore, since classical nucleation theories covering thermodynamics and kinetics laws are considered in alloy design, determining the correct choice of grain refiner is critically important. On the other hand, refining elements such as Ti, Al and Nb added to invar 36 support heterogeneous nucleation by forming new phases together with Ni, such as γ' (Ni₃Ti, Al) and γ'' (Ni₃Nb), and this makes a considerable contribution to the mechanical properties [9]. Several studies have also confirmed that the use of double refining systems (Zr-Ti, Ti-Nb, Ti-Ce, Mg-Ti, etc.) is more effective than the use of a single refiner on invar 36 [6–10]. For example, Hong-Guang et al. [6], Yu et al. [7], He et al. [10] and Chen et al. [9] reported crucial improvements in the mechanical properties of invar 36 by using double refiners: Zr-Ti, Ti-Ce, Mg-Ti, and Ti-Nb, respectively. In the study of Ti-Nb addition by Chen et al., while the average grain size was reduced from $185 \mu\text{m}$ to $101 \mu\text{m}$, the hardness of invar 36 was increased from 146.6 HV to 185.5 HV in the same case [9]. The grain refining effect on the microstructure of invar alloy and hence on its mechanical properties is clearly seen in this study.

According to previous studies in this field, it is seen that the Ti has a more impactful role as a refiner in the invar alloy especially when it is used with different elements. However, it should be noted that the CTE of invar 36 must not be disturbed while its mechanical properties have been improved. The low CTE feature is just as important as the mechanical properties in invar 36. The addition of various alloying elements (especially in macroscale) to the invar alloy can disrupt the low CTE feature by deteriorating magnetic lattice effect resulting from the magnetic moment interaction between Fe and Ni atoms. According to Weis's invar theory, it exhibits a very low CTE characteristic below the Curie temperature related to a fully austenitic crystal structure [26]. It is therefore critical that the alloying process maintain a trace amount so as not to damage the austenitic phase structure in terms of the CTE. Within the scope of our work, the effect of the Ti-Al-V triple refiner, applied for the first time to invar 36, on mechanical and physical properties was investigated in detail.

In addition, the electromagnetic interference (EMI) shielding performance of invar 36 was investigated for the first time in the frequency range 8 – 12 GHz (the X-band for radar), which is highly important for defense and aviation technologies. Fe, Ni, Co and their alloys, which are soft magnetic materials, are good candidates for EMI shielding owing to their high magnetization and low coercivity features [27–30]. Among

them, invar 36 is an inevitable material in the defense and aviation industries, where dimensional stability is essential, such as in accelerometers, and hermetic packaging, owing to its low CTE feature. In addition to the low CTE feature of invar 36, this is expected to protect electronic components inside devices such as accelerometers, from external electromagnetic waves, which may adversely affect its measurement accuracy/precision. On the other hand, EMI pollution has become an important issue not only in defense/aviation industries but also in most electronic devices (television and mobile phones etc.) because it causes device performance deterioration and human health problems.

2. Experimental 2

2.1. Materials and sample preparation 1

The samples were prepared using a 5 kg capacity VAC-LONG VISM-5 vacuum induction melting system under 10^{-4} mbar vacuum and 100 mbar partial argon gas pressure. High purity (99.99%) Ni, AISI 1008 steel and a master alloy containing 90Ti6Al4V were used to form the alloy. The melting and casting processes were repeated twice to obtain a homogeneous invar alloy. In order to avoid casting cavity defects and consequent forging cracks, castings were made in graphite moulds heated to 800°C . Three samples were prepared for this research and the coded as AC – ACHF – ACTIHF, as-cast condition, hot-forged after casting and hot forged after casting with Ti-Al-V additives, respectively. The chemical compositions were determined using a Bruker S2 PUMA X-ray fluorescence (XRF) spectrometer and the results are listed in Table 1. The ACHF and ACTIHF ingot samples were reduced in diameter from $\sim 70 \text{ mm}$ to $\sim 35 \text{ mm}$ by hot forging at 1200°C . A forging ratio of 2:1 was chosen due to the hot ductility drop phenomenon of invar 36 [31,32]. This phenomenon is called high temperature brittle intergranular fracture, and is frequently encountered in austenitic alloys such as invar 36 [31].

2.2. Characterization 3

The samples required for microstructural and grain size analysis were cut from the cross-sections of the ingots. The samples were etched with a Marble solution (50 ml HCl, 10 gr CuSO₄ and 50 ml water) for 25 seconds after grinding and polishing [33,34]. The average grain size was measured via the linear intercept technique according to the ASTM E122-13 standard from optical microscope (ZEISS Axioskop 2 MAT) images. An ImageJ programme was also used to calculate the volume fraction of twin boundaries. Firstly, the grain and twin boundaries, which were somewhat ambiguous in the optical microscope images, were clarified and transferred to ImageJ, where the total lengths of the boundaries were determined. The ratio of twin boundary length to total grain boundary length per scan field is defined as the volume fraction of twins [35,36]. The crystal structural properties of the as-prepared ingots were tested on a Rigaku MiniFlex 600 X-ray diffractometer (XRD) with Cu-K α radiation at a scan rate of $2.5^\circ/\text{min}$. In addition, the relative intensities of the XRD peaks were calculated based on the maximum peak intensity [37]. Microhardness measurements, were performed using an Emco Test DuraScan micro-tester through the microstructure samples from at least 5 points according to the Vickers HV₅ method at a load of 5 kgf (49.1 N). The room temperature tensile tests were carried out using a Zwick/Roell Z100 universal testing machine based on the ASTM standard. The thermal expansion properties of samples machined with 5 mm diameter and 20 mm length were tested using a Linseis L75 Platinum Series Dilatometer in the temperature range $20 - 150^\circ\text{C}$ at a heating rate of $3^\circ\text{C}/\text{min}$ in accordance with ASTM E228-17. The CTE of the samples was calculated according to the following CTE calculation principle (Eq. 1) based on the push-rod horizontal dilatometer method.

$$\Delta L = aL_0\Delta T \quad (1)$$

Table 1
Chemical composition of the samples (wt%).

Elements	Ni	Mn	Si	C	Ti	Al	V	Fe
AC	36.12	0.16	0.12	0.04	–	–	–	Balance
ACHF	36.12	0.16	0.12	0.04	–	–	–	Balance
ACTIHF	35.98	0.13	0.10	0.04	0.1	0.006	0.005	Balance

Where ΔL is the change in length, α is the coefficient of thermal expansion, L_0 is the original length and ΔT is the change in temperature.

The electromagnetic properties of the invar 36 were determined in the X-band microwave frequency range (8 – 12 GHz) using a rectangular transmission waveguide technique. The samples were then machined to fit the internal dimensions of the rectangular waveguide (10.16 – 22.86 mm) and to be 1 mm thick. The electromagnetic measurements of the samples were performed using an Anritsu 37397 C vector network analyzer (VNA) at room temperature. Before testing, a two-port VNA calibration was carried out, after which the magnitudes of the complex scattering parameters S11 (forward reflection coefficient) and S21 (forward transmission coefficient) were measured. Finally, the electromagnetic interference, absorption, and reflection shielding effectiveness were calculated using the scattering parameters.

3. Results and discussions

The XRD patterns of AC, ACHF and ACTIHF samples are shown in Fig. 1. All the samples had fully classic austenite (γ -Fe) XRD peaks and the strongest diffraction peaks were mainly from $\gamma(111)$, $\gamma(200)$, $\gamma(220)$,

$\gamma(311)$ and $\gamma(222)$. There are no peaks detected other than the austenite peaks in the XRD pattern because the alloying element is added in trace amounts. However, various changes in the positions of the 20 peak angles, their relative intensities and widths were observed after the processes such as hot forging and especially Ti-Al-V addition. The residual stresses that accumulated in the structure after hot deformation caused a slight shift to the right of the XRD peaks when comparing samples AC and ACHF, as shown in Fig. 1(b). On the other hand, with the addition of Ti-Al-V to invar 36, the phenomenon of shifting of the 20 peak angles became more noticeable. This shift seen in the XRD peak of the ACTIHF sample can be attributed to the more residual stresses that are generated in the structure after hot forging. Different sized elements contained in the alloy, such as Ti, Al and V, further distort the crystal lattice by creating additional microstrains throughout the forging process. It is well known that the FCC crystal lattice has a closed package structure and, accordingly, the lattice distortion results from the different atoms in the FCC lattice being placed as solid solution atoms [38]. According to the Bragg equation ($\lambda = 2dsin\theta$), the shift of the diffraction peaks to high angles indicates a decrease in the crystal plane spacing and lattice parameter [39,40]. A similar phenomenon occurs in metals that have

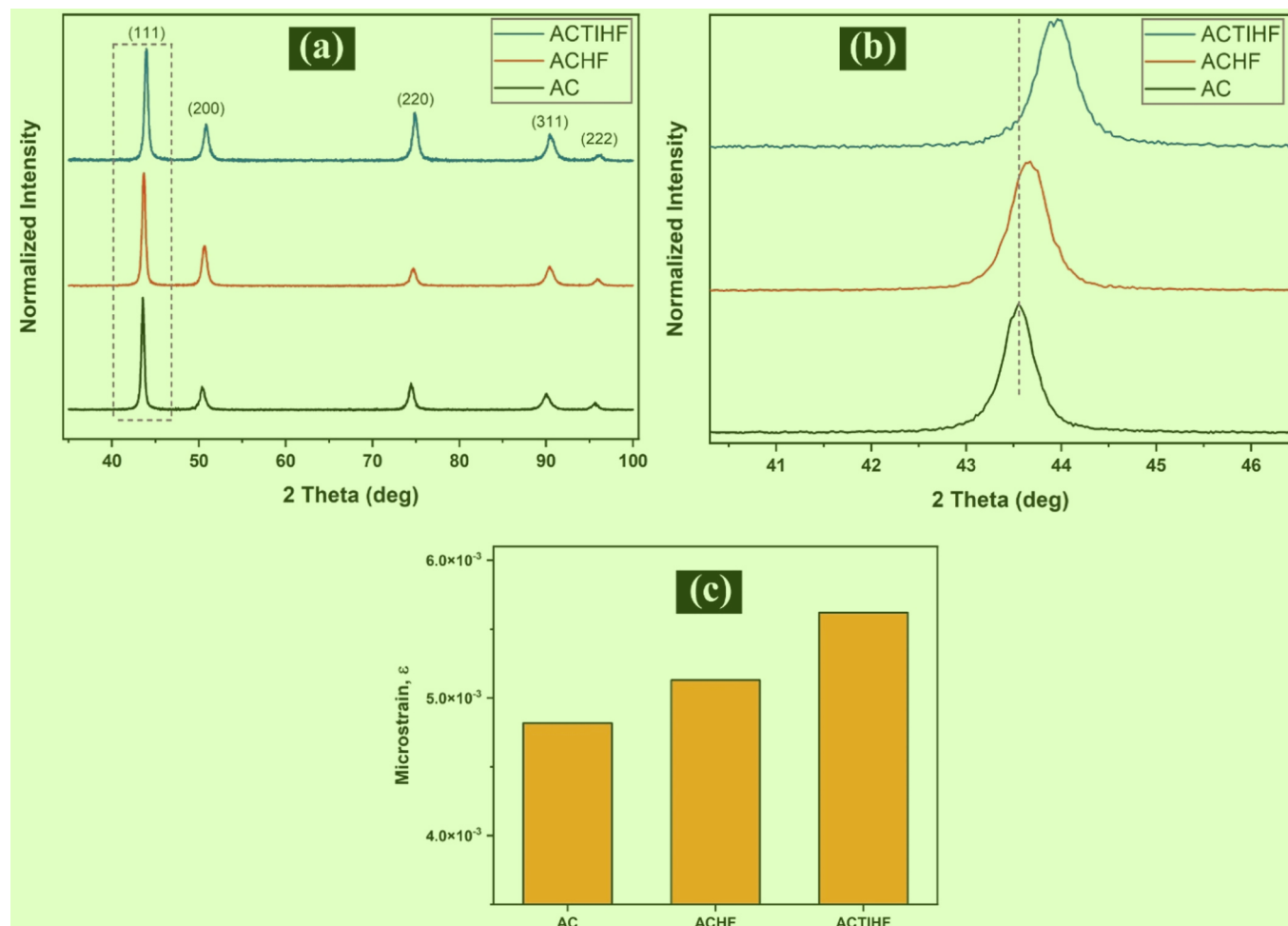


Fig. 1. (a) Normalized XRD patterns of the invar alloys, (b) the strongest (111) XRD peak shift, and (c) microstrain values.

undergone severe plastic deformation, known as the residual stress and microstrain effect [41,42]. However, it is well known that atomic sizes of Ti, V and Al (0.147 nm, 0.179 nm, and 0.143 nm respectively) are larger than atomic sizes of Fe and Ni (0.126 nm and 0.124 nm respectively). In fact, while the 2-theta angle is expected to shift to the left, a shift to the right is observed. As the alloying is only present in trace amounts, it is understood that the effect of residual stresses and microstrain are more dominant. There is a significant reduction in grain size with the addition of the refiner, which can mean more grain boundaries in the structure and consequently more microstrains. This can be attributed to more residual stress in the structure due to the addition of alloying elements and the effect of deformation and increase in microstrain at the lattice structure [43]. The microstrain values of the samples presented in Fig. 1(c) were calculated using the Williamson-Hall approach, as described by Eq. 2 below [44]. It can be observed that microstrain values increase as a result of both hot forging and the refiner.

$$\varepsilon = \frac{\beta}{4\tan\theta} \quad 1 \quad (2)$$

Where ε microstrain, β full width at half maximum (FWHM) in radians, and θ peak position in radians.

As the peaks obtained from the XRD analysis are characteristic of the austenite phase and there is no other peak, the XRD pattern have been normalized. Normalized XRD pattern is used in particular to compare relative peak intensities. The relative intensity variations of the samples listed in Table 2 were calculated based on the intensity of the maximum peak (111). It can be seen that the relative intensities of thermodynamically stable planes such as (111) were higher in the all samples, in natural. Generally, the FCC metals are crystallized during solidification in the preferred directions, which is the further intensity of the atoms, to minimize the surface energy [45]. As known, the surface energy of (111) crystal plane is lower than others in the FCC metals [46,47]. Therefore, the (111) crystal plane, which has the lower surface energy, is thermodynamically more dominant in all cases. However, it can be seen that the various crystal planes are oriented with a recrystallization and twin effect resulting from hot deformation, and also with an alloying elements effect [48]. When AC and ACHF samples were compared, the intensity of peak (200) increased significantly while the intensity of the other peaks decreased after hot forging. This can be attributed to the recovery and recrystallisation of the metal microstructure under the influence of temperature and force during hot forming as a result of increased diffusion kinetics [49,50]. A similar phenomenon was observed in the study by Sato et al. [51]. It is important to note that no complete recovery and recrystallisation occurred following hot forging. This is because, although the forging process is carried out at a high temperature, additional heat treatment is necessary for complete recrystallisation in accordance with ASTM standards [52]. Consequently, the observed changes in XRD peak intensities are also related to the preferential rotation of the grains during the forging process. On the other hand, it is interesting to note that the density of (220) showed a significant increase with the addition of the Ti-Al-V refiner. In the comparison of the ACHF and ACTIHf samples, no significant change in intensity was observed in the (200) and (222) planes, while a significant orientation was observed in the (220) and (311) planes.

Fig. 2 shows the optical microscope (OM) images of the AC, ACHF and ACTIHf samples. Rather coarse grains were formed after casting in the AC sample with a size of $\sim 500 \mu\text{m}$, as can be seen in Fig. 2(a). It is

well known that the solidification of molten metal in a mould first starts at the wall with a nucleation phenomenon. The growth of the formed nuclei continues from the mould wall in the direction opposite to the removal of heat [4,24]. Thus, the final grain size generated as a result of the ingot casting process depends on the heat dissipation rate of the molten metal. The solidification rate of traditional ingot casting in a refractory-based mould (sand, etc.) is close to thermodynamically stable cooling rates, resulting in the formation of relatively coarse grains [53]. These ingots, which have coarse grains after casting, are not used in directly in an application due to various possible casting defects (gas or shrinkage cavities, etc.) and poor mechanical properties. That's why the ingots are subjected to various hot forming processes, such as forging or rolling, to obtain an intermediate product in a form of sheet or rod, and also to eliminate any casting defects. Particularly during the hot forging process, as shown in Fig. 2(b), the coarse grain size after casting was refined by the effect of recrystallization and dynamic force. Therefore, the grain size after forging in the ACHF sample decreased from $500 \mu\text{m}$ to $100 \mu\text{m}$. In addition to these, the deformation twins commonly encountered in FCC structures were formed during the forging process, as shown in Fig. 2(b and c). In this way, both grain refinement through the triple microalloying process and twin formation through hot forging contribute significantly to the improvement in the mechanical properties. Fig. 2(d and e) shows the images used in the Image J programme to calculate the volume fraction of twin boundaries. According to Wang et al., the ratio of twin boundaries to grain boundaries determines the volume fraction of twin boundaries within the structure [35,36]. As a result of calculations made using the ImageJ programme, the density of twin boundaries, which was 32.1% in the ACHF sample, increased to 40.2% in the ACTIHf sample due to the refiner effect.

In general, the refiners provide an extra nucleation center in addition to the mould walls, which allows solidification to begin, and as can be seen in Fig. 3, the grain size were become finer. It was seen in Fig. 2(c) that the average grain size was reduced up to $40 \mu\text{m}$. As can be seen from the EDS mapping analysis in Fig. 3, high melting particles such as TiC ($\sim 3160^\circ\text{C}$) and Al_2O_3 ($\sim 2050^\circ\text{C}$) made a significant contribution to the average grain size reduction by forming extra nucleation centres during solidification. It is well known that the carbon atoms have a greater affinity for the titanium atoms and the TiC is the most stable phase, while the aluminum atoms have a strong affinity for the oxygen atoms, resulting in the formation of a highly stable Al_2O_3 phase [54–56]. In addition to these, the Ti-Al-V addition had a significant impact on the dynamic recrystallization (DRX) mechanism during hot forging. In a study in which Ti-Mg was added to invar 36, He et al. reported that the DRX mechanism is the more dominant driving force, especially at temperatures above 800°C [10].

The CTE results of the samples are shown in Fig. 4. Firstly, when the refiner-free AC and ACHF samples are considered, the CTE decreased from $1.86 \times 10^{-6}/^\circ\text{C}$ to $1.15 \times 10^{-6}/^\circ\text{C}$ in the temperature range of $20 - 100^\circ\text{C}$ with the hot forging process. This situation can be clarified with two different approaches. The first of these, the grain boundary intensity in the structure increases considerably as a result of grain size reduction after forging, and deformation twins and their boundaries have also been revealed. The grain and twin boundaries inhibit lattice vibration, which is thermally responsible for the expansion of solids [57]. It is well known that lattice vibrations in solids increase with temperature, and this way increased atomic mobility makes thermal expansion easier [2, 23]. Thus, in general, factors such as grain or twin boundaries that can restrict lattice vibrations can provide a lower CTE. According to the invar theory, the low CTE characteristic of invar 36 is primarily a function of magneto-volume contraction, but lattice vibrations are naturally still present and contribute to its thermal expansion [2,4]. In addition, the residual stresses formed after hot forging also play a restrictive role in lattice vibration or atomic mobility. Therefore, more grain boundaries, higher dislocation densities and residual stresses, which are formed by hot forging, contributed to the reduction in the CTE by limiting lattice vibrations [2,4]. This could be the reason for the

Table 2
The strongest XRD peaks variation in relative intensity (%).

Strongest Peak	(111)	(200)	(220)	(311)	(222)
AC	100	21.25	23.29	15.09	7.24
ACHF	100	35.85	15.89	17.62	6.39
ACTIHf	100	33.33	43.16	24.43	5.84

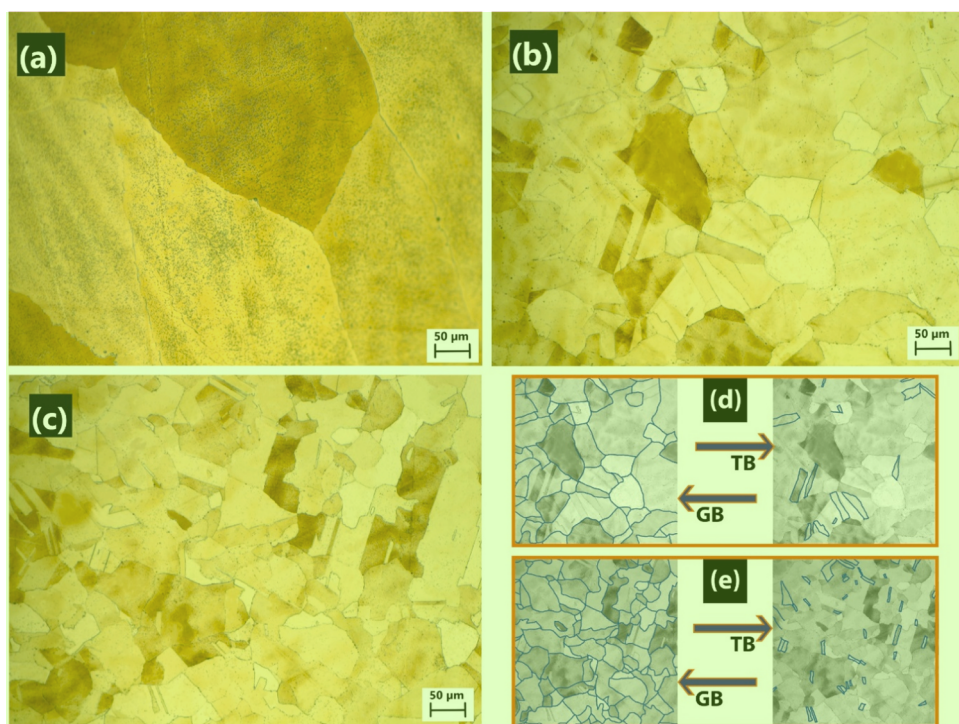


Fig. 2. Optical microstructure images of the a) AC, b) ACHF and c) ACTIHf samples and, d) ACHF and e) ACTIHf samples grain boundaries (GB) and twin boundaries (TB).

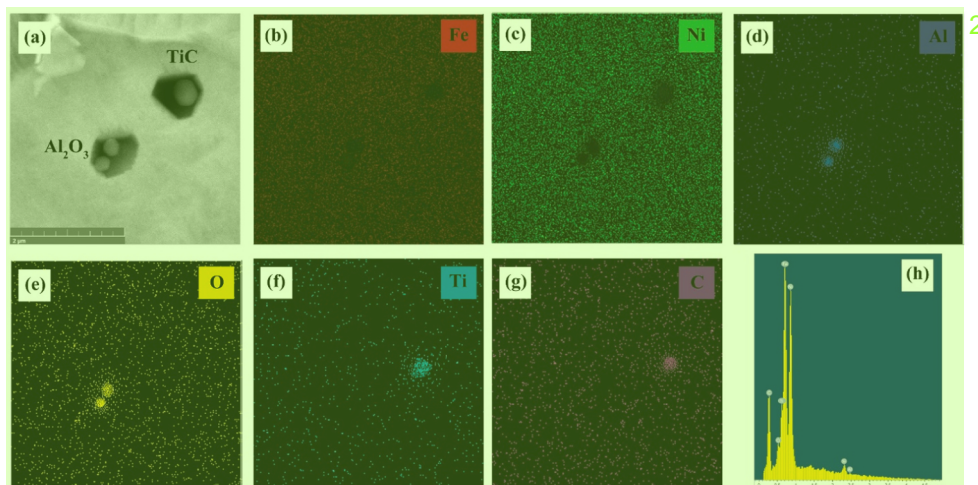


Fig. 3. The typical second-phase particles in ACTIHf alloy: (a) the typical morphology of TiC and Al₂O₃ particles; (b – g) corresponding EDS mapping images of Fe, Ni, Al, O, Ti and C in ACTIHf alloy, respectively; (h) corresponding EDS results from (a).

decrease in the CTE with the hot forging process. Magnetic volume contraction and thermally induced lattice expansion can be affected by residual stresses associated with forging. It can also vary the interatomic distance and disturb the balance in the magnetic lattice structure, subsequently contributing to exchange interspin interactions [58–60]. It is understood that there is a difference between the as-cast interatomic distance and the hot-forged interatomic distance. It is understood that the interatomic distances of the as-cast and hot-forged samples are different. Given that any micro-porosity formed throughout the casting was closed after forging, the balance in the magnetic lattice structure and, accordingly, the exchange interspin interactions could vary [60]. This case is supported by a slight shift to larger angles of the XRD diffraction peak, also shown in Fig. 1(b). These small variations in the crystal plane spacing and lattice parameters affect the lattice vibration

and the mobility of atoms and are more pronounced in the CTE, especially at low temperatures, as shown in Fig. 4. On the other hand, the differences in the CTEs of the ACHF and ACTIHf samples can be attributed to isotropic CTE behavior. As can be seen from the XRD results of the ACTIHf sample, the intensities of the (220) and (311) planes have been orientated with a significant increase. Correspondingly, the intensities of the other planes are reduced. The differences in the crystal plane directions cause changes in the elastic modulus and accordingly thermal expansion. It is well known that thermal expansion depends on thermal stress and elastic stretching of the crystal lattice [61]. In addition, the thermal expansion is generally low in directions where the elastic modulus is high. Considering that the elastic modulus of the (111) plane is higher in the FCC austenite crystalline, it can be said that there are preferential crystallographic orientations associated with the

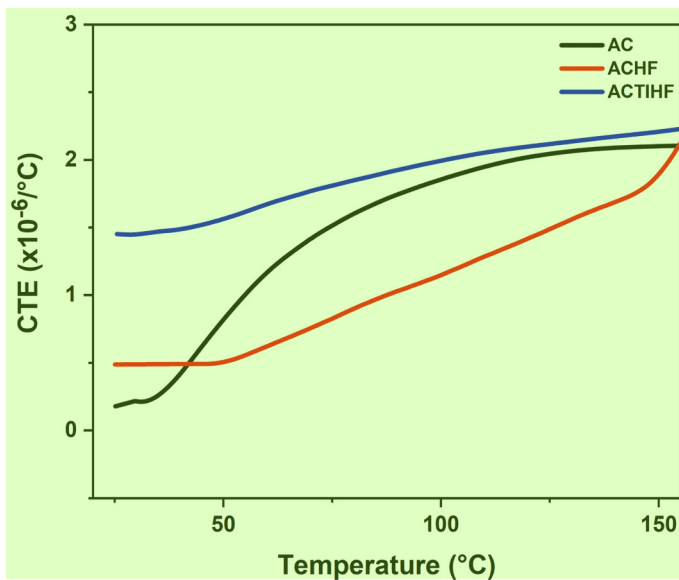


Fig. 4. CTE results of the samples. 2

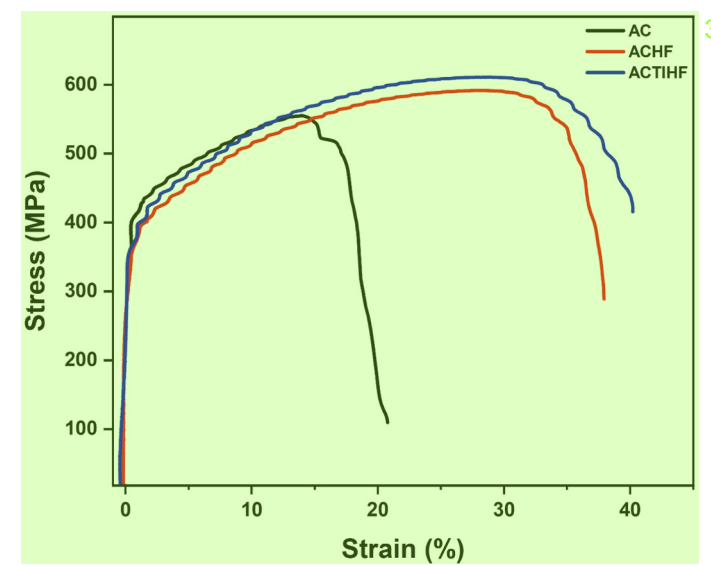
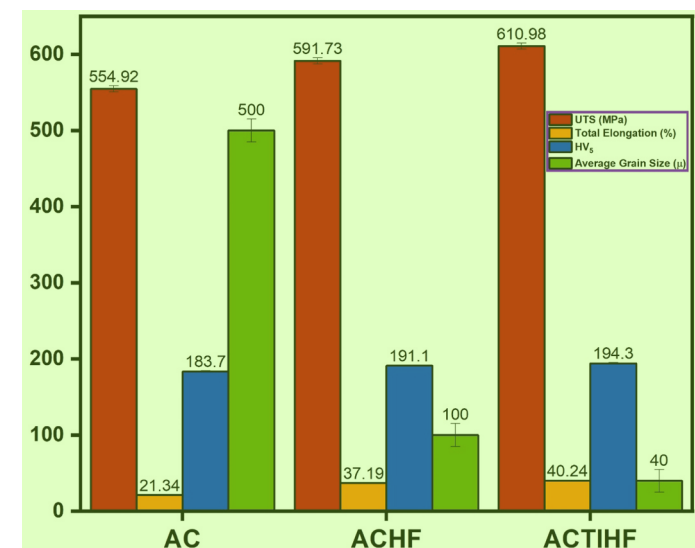


Fig. 5. Stress – Strain curves of the samples. 3

addition of Ti-Al-V at this plane intensity, and consequently, the CTE increases [37]. Although the CTE of the Ti-Al-V alloy sample is higher than that of the other sample, it has a more stable CTE characteristic as shown in Fig. 4. In general, preferential orientations tend to occur in specific crystal-dependent planes, where sliding is easier [62]. As a result of this, an isotropic CTE behavior may have emerged. In addition, part of the Ti, Al and V atoms could have formed a solid solution in the austenitic FCC phase as a substituent atom. Therefore, the FCC lattice order can be distorted in the form of substitutional or interstitial Ti, Al and V atoms. In fact, the main issue associated with the increase in the CTE with the introduction of alloying elements is related to the distortion of the specific magnetic lattice structure in Fe36Ni. In addition, the formation of heterogeneous nucleation centres (intermetallic compounds or oxides) in the austenite matrix can also cause distortion of the FCC lattice. All of these phenomena can slightly vary the interatomic distance, disturbing the balance in the magnetic lattice structure and contributing to the exchange of interspin interactions (Fe-Fe, Fe-Ni and Ni-Ni) [58,59]. The magneto-lattice effect, which arises from the magnetic moment interactions between Fe and Ni atoms in the lattice, could be partially destroyed by the dissolution of alloying elements in the invar matrix. Even though no other phase other than austenite phase was detected in the XRD analysis, as can be seen in Fig. 1(b), there was a significant shift to larger angles at certain peak diffraction points with the addition of the Ti-Al-V triple refiner.

The tensile test results of the samples are shown in Fig. 5 and the values for ultimate tensile strength (UTS), hardness and average grain size are shown in Fig. 6. Accordingly, higher UTS and hardness values of 610.9 MPa and 194.3 HV₅, respectively, were obtained for the Ti-Al-V added sample (ACTIHF). As shown in Fig. 5 and Fig. 6, the mechanical properties of the AC sample, both in terms of UTS, hardness and especially total elongation, were minimal. In the case of the ACHF sample, the total elongation and UTS considerably increased after the hot forging process. This difference between the two samples (AC and ACHF) can be attributed to the fact that hot forging eliminates possible casting defects in the ingots and reduces the grain size. It is well known that defects such as micro-shrinkage or gas cavities can often occur after the casting process [63]. Such casting cavity defects can act as stress accumulation centres during tensile testing [63]. Thus, as shown in Fig. 5, a sudden failure with a minimal amount of elongation could occur unexpectedly. In addition, the dynamic recrystallisation mechanism played an active role in grain size reduction during the hot forging process. Invar 36 has a medium stacking fault energy ($\gamma_{\text{SFE}} =$

Fig. 6. The UTS, total elongation, hardness (HV₅) and average grain size results of the samples under different conditions. 1

122 mJ/m²) accordingly, the dislocation density can easily increase to a high level by hot forging, resulting in localized dislocation density variations [3,4,64]. These localized dislocation density variations are considered as the driving force for the nucleation of new grains, and their quantities are also high enough to facilitate long-range migration of high-angle boundaries [64]. For this reason, discontinuous dynamic recrystallization can be assumed to be responsible for the reduction in the grain size of invar 36 during deformation and the resulting increase in strength. 4

On the other hand, Fig. 6 shows that with the addition of the Ti-Al-V triple refiner, the grain size continues to decrease and the tensile strength, hardness and total elongation increase accordingly. A comparison of the ACHF and ACTIHF specimens revealed that the UTS, hardness and total elongation increased from 591.7 MPa to 610.9 MPa, from 191.1 HV₅ to 194.3 HV₅ and from 37.1% to 40.2%, respectively, while the average grain size decreased from 100 μm to 40 μm. A reduction in grain size due to the addition of a refiner also indicated that the grain boundaries, which are mainly responsible for the increase in mechanical properties, occupied a considerable amount of space in the

structure. As the grain boundaries are the regions that limit dislocation movement, it is expected that the strength and hardness will improve as their proportion in the structure increases. This is because the different orientations of the grains make it difficult for dislocations to pass from one grain to another [64]. Dislocation movements are also complicated by discontinuities in the slip plane of each grain. When all these factors are considered together, the improvement in strength in the ACTIHC sample is strongly related to the grain-boundary strengthening or Hall-Petch strengthening mechanism.

Fig. 7(a) shows the reflection (R), transmission (T) and absorption (A) coefficient curves of invar 36 (ACHF sample), which illustrate the material's response to the incident wave, i.e., the proportion of absorption, reflection, and transmission. The S parameters (S_{11} and S_{21}) of invar 36 were determined using a vector network analyzer. Reflection and transmission coefficients can be calculated from the relations $R = |S_{11}|^2$ and $T = |S_{21}|^2$ using the reflection and absorption scattering parameters. The absorption coefficient (A) was calculated using the

equation $A + R + T = 1$ [27,65]. The general mechanism in conductive materials is reflection due to the abundance of mobile charge carriers that interact with electromagnetic fields [27]. A clearly high reflection coefficient and very extremely poor transmission coefficient, with the lowest absorption coefficient, were observed throughout the X-band for invar 36. The free electrons in ferromagnetic metals are supposed to aid in surface reflection [65]. The fact that invar 36 is a soft magnetic material with low coercivity (~ 24 A/m) and high electrical conductivity (12500 S/cm at room temperature) and is one of the most important factors for providing good reflection and absorption parameters [63,66]. Near-zero T, relatively high A and high R values indicate that invar 36 is relatively absorptive of EM waves in the material and provides EMI shielding through significant reflection even at a 1 mm thickness.

Fig. 7(b) shows the total (SE_T), reflection (SE_R) and absorption (SE_A) shielding efficiency curves of invar 36. The total shielding effectiveness represents the combination of reflection and absorption shielding effectiveness. In fact, the total shielding effectiveness is $SE_T = SE_R + SE_A$

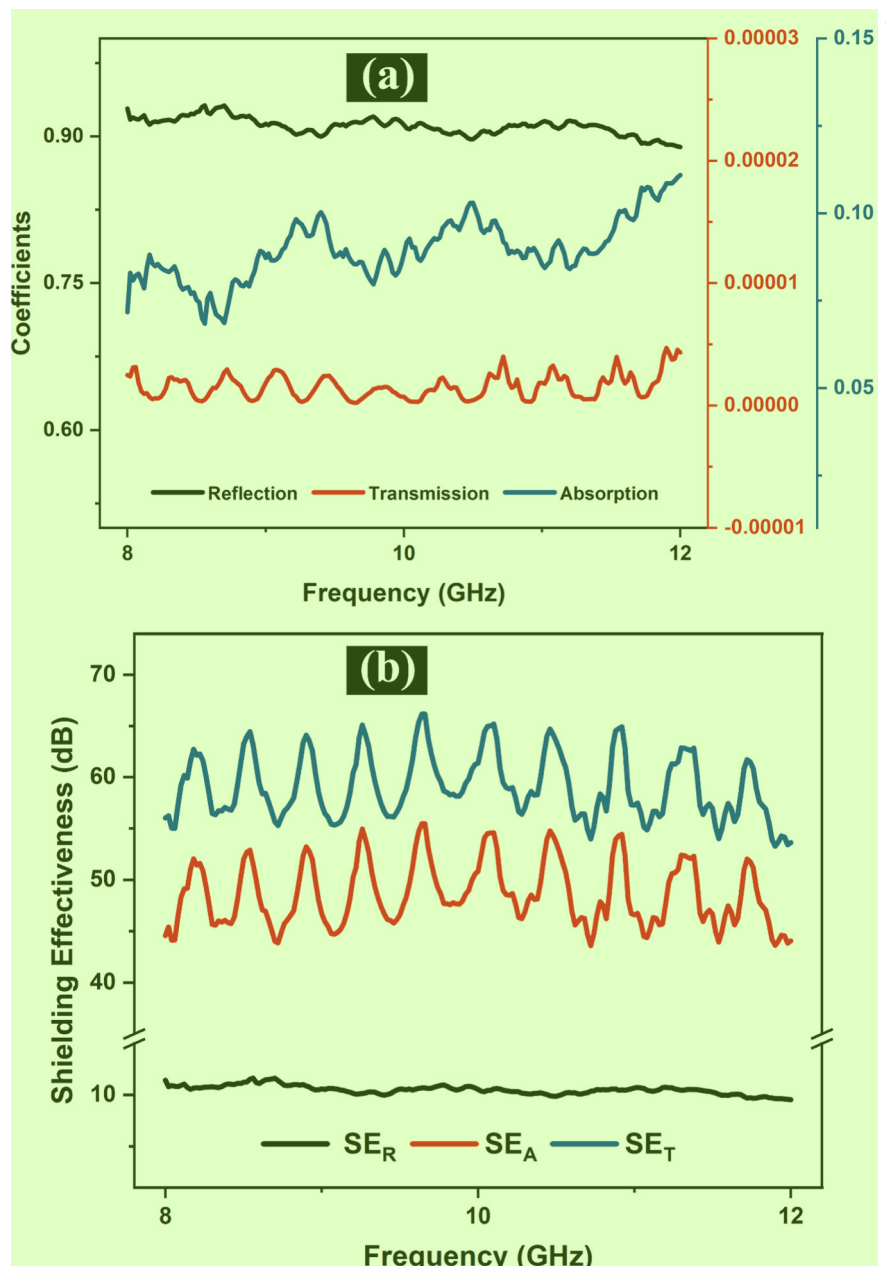


Fig. 7. (a) Transmission, absorption and reflection coefficients of invar 36 and (b) the total EMI shielding effectiveness (SE_T), reflection shielding effectiveness (SE_R) and absorption shielding effectiveness (SE_A) for invar 36.

+ SE_M . However, SE_M usually involves multiple internal reflections considered for certain design geometries, such as porous and ultra-thin structures [27,65]. In addition, the SE_M contribution can be neglected under the conditions of $SE_T > 15$ dB, $SE_A > 10$ dB or plane waves containing electric fields [29,65]. Since the shielding test sample is a high-density bulk alloy of sufficient thickness (1 mm), the SE_M is ignored in the present study. The reflection shielding efficiency (SE_R) and the absorption shielding efficiency (SE_A) are calculated from the reflection and transmission coefficients as given in the equations below:

$$SE_R = -10\log(1-R) \quad 1 \quad (3)$$

$$SE_A = -10\log\left(\frac{T}{1-R}\right) \quad (4)$$

The bulk invar 36 with a thickness of 1 mm showed total shielding in the range of -55 dB to -65 dB. Fig. 6(b) shows that the contribution of the reflection component to the shielding effectiveness is -10 dB, while the contribution of the absorption component is -50 dB. The high magnetic permeability ($\mu_{max} = 6000$) and good electrical conductivity of invar 36 are responsible for this high shielding effectiveness of ~ 60 dB [63,66]. Reflection, the primary mechanism of protection for metallic materials, is explained by the abundance of free electrons in metals so that the incident EM wave on the material is reflected between the air and the surface. With respect to the absorbing mechanism, it is well known that when an EM wave penetrates a metallic material, a micro-current is generated inside the material and this phenomenon makes an important contribution to EM wave absorption [67]. As a result, it is understood that the 1 mm thick bulk invar 36 provides significant shielding against X-band EM waves.

4. Conclusions 3

The effects of Ti-Al-V triple microalloying and hot forging on the microstructure, mechanical, and physical properties of invar 36 were studied in detail. The electromagnetic interference (EMI) shielding characteristics of plain invar 36 have also been investigated for the first time.

- i. All the samples have fully classical austenite (γ -Fe) XRD peaks. The main diffraction peaks are $\gamma(111)$, $\gamma(200)$, $\gamma(220)$, $\gamma(311)$ and $\gamma(222)$. While a slight shift to the right was observed in the XRD peaks due to the deformation-induced residual stresses, this shifting phenomenon became more pronounced with the addition of Ti-Al-V to invar 36. Considering the relative intensity of the samples, the (220) and (311) planes were oriented after the addition of the Ti-Al-V refiner.
- ii. The average grain size of the samples was reduced from 500 μm to 100 μm by hot forging. A further reduction from 100 μm to 40 μm was achieved by Ti-Al-V triple refining.
- iii. The coefficient of thermal expansion of the samples was decreased from $1.86 \times 10^{-6}/^{\circ}C$ to $1.15 \times 10^{-6}/^{\circ}C$ in the temperature range of $20 - 100$ $^{\circ}C$ due to various factors such as grain and twin boundaries, that formed as a result of hot forging. These boundaries and residual stresses have had a limiting effect on the lattice vibration, which is the main reason for the low CTE. However, the increase in the CTE of the sample with added Ti-Al-V was related to the distortion of the balance in the specific magnetic lattice structure and the change in interatomic distance.
- iv. The best tensile strength, hardness and total elongation were obtained for the sample with added Ti-Al-V, at 610.9 MPa, 194.3 HV₅ and 40.2% , respectively, which are directly related to the grain boundary strengthening mechanism.
- v. Bulk invar 36 with a thickness of 1 mm exhibited a total shielding in the range of -55 dB to -65 dB, as indicated by the contribution of the reflection (~ 10 dB) and absorption (~ 50 dB) components. Invar 36 has a very high reflection coefficient and an

extremely poor transmission coefficient, with the lowest absorption, throughout the X-band.

CRediT authorship contribution statement 5

Mehmet Kul: Project administration, Methodology, Investigation, Conceptualization. **Bekir Akgül:** Writing – review & editing, Writing – original draft, Visualization, Validation, Supervision, Resources, Project administration, Methodology, Investigation, Formal analysis, Data curation, Conceptualization. **Yusuf Ziya Karabay:** Writing – review & editing, Supervision, Project administration, Methodology. **Kaan Pehlivanoğlu:** Validation, Resources, Formal analysis, Data curation, Conceptualization. **Bahadır Türkyaman:** Resources, Methodology, Data curation.

Declaration of Competing Interest 2

The authors declare that they have no known competing financial interests or personal relationships that could have appeared to influence the work reported in this paper.

Data availability 6

Data will be made available on request. 9

Acknowledgments 1

This research is supported by the Scientific and Technological Research Council of Türkiye (TUBITAK) (Grant No. 123M286). The authors thank to TUBITAK for their supports. The authors are also grateful for the fellowship support of the TUBITAK Directorate of Science Fellowships and Grant Programs (BİDEB).

References 4

- [1] C.E. Guillaume, Recherches sur les aciers au nickel. Dilatations aux températures élevées; résistance électrique. *C. R. Acad. Sci. Paris* 125 (1897) 235–238.
- [2] B. Akgül, M. Kul, F. Erden, The puzzling thermal expansion behavior of invar alloys: a review on process-structure-property relationship, *Crit. Rev. Solid State Mater. Sci.* (2023) 1–54, <https://doi.org/10.1080/10408436.2023.2170975>.
- [3] J.-J. Zheng, C.-S. Li, S. He, B. Cai, Y.-L. Song, Microstructural and tensile behavior of Fe-36%Ni alloy after cryorolling and subsequent annealing, *Mater. Sci. Eng. A* 670 (2016) 275–279, <https://doi.org/10.1016/j.msea.2016.06.004>.
- [4] M. Kul, B. Akgül, Y.Z. Karabay, The relationship of hot and cold rolling processes with the structure and properties of invar 36, *Mater. Chem. Phys.* 295 (2023) 127215, <https://doi.org/10.1016/j.matchemphys.2022.127215>.
- [5] J. Zhang, Y. Tu, J. Xu, J. Zhang, J. Zhang, Effect of solid solution treatment on microstructure of Fe-Ni based high strength low thermal expansion alloy, *J. Iron Steel Res. Int.* 15 (2008) 75–78, [https://doi.org/10.1016/S1006-706X\(08\)60016-3](https://doi.org/10.1016/S1006-706X(08)60016-3).
- [6] Z. Hong-Guang, Y. Li-Jiang, X. Heng, Effect of two kinds of refiners on the solidification structure and property of invar alloy, *High. Temp. Mater. Process.* (2013) <https://doi.org/10.1515/htmp-2012-0153>.
- [7] Y. Yu, W. Chen, H. Zheng, Effects of Ti-Ce refiners on solidification structure and hot ductility of Fe-36Ni invar alloy, *J. Rare Earths.* (2013), [https://doi.org/10.1016/S1002-0721\(12\)60381-0](https://doi.org/10.1016/S1002-0721(12)60381-0).
- [8] S.M. Abbasi, M. Morakabati, R. Mahdavi, A. Momeni, Effect of microalloying additions on the hot ductility of cast FeNi36, *J. Alloy. Compd.* (2015), <https://doi.org/10.1016/j.jallcom.2015.03.167>.
- [9] C. Chen, B. Ma, B. Liu, J. He, H. Xue, Y. Zuo, X. Li, Refinement mechanism and physical properties of arc melted invar alloy with different modifiers, *Mater. Chem. Phys.* (2019), <https://doi.org/10.1016/j.matchemphys.2019.02.006>.
- [10] Y. He, F. Wang, C. Li, Z. Yang, J. Zhang, Y. Li, Effect of Mg content on the hot ductility of wrought Fe-36Ni alloy with Ti addition, *Mater. Sci. Eng. A.* (2016), <https://doi.org/10.1016/j.msea.2016.07.070>.
- [11] I.K. Bitkulov, A.M. Burkhanov, V.A. Kazantsev, R.R. Mulyukov, K.Y. Mulyukov, I. M. Safarov, Effect of severe plastic deformation on the properties of the Fe-36% Ni invar alloy, *Phys. Met. Metallogr.* 102 (2006) 91–96, <https://doi.org/10.1134/S0031918806070131>.
- [12] A. Vinogradov, S. Hashimoto, V.I. Kopylov, Enhanced strength and fatigue life of ultra-fine grain Fe-36Ni Invar alloy, *Mater. Sci. Eng. A.* (2003), [https://doi.org/10.1016/S0921-5093\(03\)00082-0](https://doi.org/10.1016/S0921-5093(03)00082-0).
- [13] Z. Eliezer, J.T. Hoggins, Plastic deformation of invar alloys, *Mater. Res. Bull.* (1977), [https://doi.org/10.1016/0025-5408\(77\)90139-8](https://doi.org/10.1016/0025-5408(77)90139-8).

- [14] H.-Y. Song, G.-D. Wang, H.-T. Liu, Effect of cold rolling on microstructure and texture evolution in strip casting Fe-36Ni invar alloy foil, *J. Alloy. Compd.* 888 (2021) 161519, <https://doi.org/10.1016/j.jallcom.2021.161519>.
- [15] K. Nakama, K. Sugita, Y. Shirai, Effect of MC type carbides on age hardness and thermal expansion of Fe-36 wt%Ni-0.2 wt%Cr Alloy, *Metallogr. Microstruct. Anal.* 2 (2013) 383–387, <https://doi.org/10.1007/s13632-013-0101-9>.
- [16] H. Liu, Z. Sun, G. Wang, X. Sun, J. Li, F. Xue, H. Peng, Y. Zhang, Effect of aging on microstructures and properties of Mo-alloyed Fe-36Ni invar alloy, *Mater. Sci. Eng. A.* 654 (2016) 107–112, <https://doi.org/10.1016/j.msea.2015.12.018>.
- [17] Q. Sui, J. He, X. Zhang, Z. Sun, Y. Zhang, Y. Wu, Z. Zhu, Q. Zhang, H. Peng, Strengthening of the Fe-Ni Invar Alloy Through Chromium, *Mater. (Basel)* 12 (2019) 1297, <https://doi.org/10.3390/ma12081297>.
- [18] Q.S. Sui, J.X. Li, Y.Z. Zhai, Z.H. Sun, Y.F. Wu, H.T. Zhao, J.H. Feng, M.C. Sun, C. L. Yang, B.A. Chen, H.F. Peng, Effect of alloying with V and Ti on microstructures and properties in Fe-Ni-Mo-C invar alloys, *Materialia* (2019), <https://doi.org/10.1016/j.mtla.2019.100474>.
- [19] M.F. Kılıçaslan, Y. Yılmaz, B. Akgül, H. Karataş, C.D. Vurdu, Effect of Fe-Ni substitution in FeNiSIB soft magnetic alloys produced by melt spinning, *Adv. Mater. Sci.* 21 (2021) 79–89, <https://doi.org/10.2478/adms-2021-0026>.
- [20] M.F. Kılıçaslan, S.I. Elburnı, B. Akgül, The effects of Nb addition on the microstructure and mechanical properties of melt spun Al-7075 alloy, *Adv. Mater. Sci.* 21 (2021) 16–25, <https://doi.org/10.2478/adms-2021-0008>.
- [21] H. Van Swygenhoven, Grain boundaries and dislocations, *Sci. (80-.)* 296 (2002) 66–67, <https://doi.org/10.1126/science.1071040>.
- [22] N. Hansen, Hall-Petch relation and boundary strengthening, *Scr. Mater.* 51 (2004) 801–806, <https://doi.org/10.1016/J.SCRIPTAMAT.2004.06.002>.
- [23] W.D. Callister, D.G. Rethwisch. *Materials Science and Engineering: An Introduction*, 10th ed., Wiley, 2018.
- [24] M. Kul, B. Akgul, K.O. Oskay, A.E. Alsanc, B. Karaca, Optimisation of recycled moulding sand composition using the mixture design method, *Int. J. Cast. Met. Res.* 34 (2021) 104–109, <https://doi.org/10.1080/13640461.2021.1936381>.
- [25] T.K. Ha, S.H. Min, Effect of C content on the microstructure and physical properties of Fe-36Ni invar alloy, *Mater. Sci. Forum* 804 (2014) 293–296, <https://doi.org/10.4028/www.scientific.net/MSF.804.293>.
- [26] R.J. Weiss, The origin of the “invar” effect, *Proc. Phys. Soc.* (1963), <https://doi.org/10.1088/0370-1328/82/2/314>.
- [27] K.S. Dijith, R. Aiswarya, M. Praveen, S. Pillai, K.P. Surendran, Polyol derived Ni and NiFe alloys for effective shielding of electromagnetic interference, *Mater. Chem. Front.* 2 (2018) 1829–1841, <https://doi.org/10.1039/C8QM00264A>.
- [28] B.-W. Li, Y. Shen, Z.-X. Yue, C.-W. Nan, Enhanced microwave absorption in nickel/hexagonal-ferrite/polymer composites, *Appl. Phys. Lett.* 89 (2006), <https://doi.org/10.1063/1.2357565>.
- [29] P. Murugaiyan, A. Mitra, A.K. Panda, A.S. Kumar, R.K. Roy, K. Manna, S. K. Srivastava, Electromagnetic interference shielding effectiveness of amorphous and nanocomposite soft magnetic ribbons, *Phys. B Condens. Matter* 568 (2019) 13–17, <https://doi.org/10.1016/j.physb.2019.05.017>.
- [30] J. Liu, M.-S. Cao, Q. Luo, H.-L. Shi, W.-Z. Wang, J. Yuan, Electromagnetic property and tunable microwave absorption of 3D nets from nickel chains at elevated temperature, *ACS Appl. Mater. Interfaces* 8 (2016) 22615–22622, <https://doi.org/10.1021/acsmami.6b05480>.
- [31] L. Ben Mostefa, G. Saindrenan, M.P. Solignac, J.P. Colin, Effect of interfacial sulfur segregation on the hot ductility drop of FeNi36 alloys, *Acta Metall. Mater.* (1991), [https://doi.org/10.1016/0956-7151\(91\)90044-2](https://doi.org/10.1016/0956-7151(91)90044-2).
- [32] Y. Yanchong, C. Weiqing, Z. Hongguang, Research on the hot ductility of Fe-36Ni invar alloy, *Rare Met. Mater. Eng.* 43 (2014) 2969–2973, [https://doi.org/10.1016/S1875-5372\(15\)60044-3](https://doi.org/10.1016/S1875-5372(15)60044-3).
- [33] H. Gu, C. Wei, L. Li, M. Ryan, R. Setchi, Q. Han, L. Qian, Numerical and experimental study of molten pool behaviour and defect formation in multi-material and functionally graded materials laser powder bed fusion, *Adv. Powder Technol.* 32 (2021) 4303–4321, <https://doi.org/10.1016/j.apt.2021.09.036>.
- [34] J.R. Davis (Ed.), *Nickel, Cobalt, and Their Alloys*, ASM International, 2000.
- [35] Q. Wang, Y. Dong, Z. Jiang, J. Huang, Effects of trace additions of magnesium on microstructure and properties of Fe-36Ni Invar alloy, *Steel Res. Int.* 94 (2023), <https://doi.org/10.1002/srin.202300047>.
- [36] Q. Wang, Y. Dong, Z. Jiang, T. Zou, Y. Liu, Y. Wu, H. Qing, Effects of Ce addition on mechanical properties and thermal expansion behavior of Fe-36Ni Invar alloy, *Mater. Charact.* 207 (2024) 113584, <https://doi.org/10.1016/j.matchar.2023.113584>.
- [37] Q. Zhao, Y. Wu, J. He, Y. Yao, Z. Sun, H. Peng, Effect of cold drawing on microstructure and properties of the invar alloy strengthened by carbide-forming elements, *J. Mater. Res. Technol.* 13 (2021) 1012–1019, <https://doi.org/10.1016/j.jmrt.2021.05.026>.
- [38] S. Praveen, B.S. Murty, R.S. Kottada, Alloying behavior in multi-component AlCoCrCuFe and NiCoCrCuFe high entropy alloys, *Mater. Sci. Eng. A.* 534 (2012) 83–89, <https://doi.org/10.1016/j.msea.2011.11.044>.
- [39] S. Zhong, M. Yang, S.U. Rehman, S. Luo, L. Li, C. Li, J. Li, S. Xiong, I. Bulyk, B. Yang, Optimization of core-shell structure distribution in sintered Nd-Fe-B magnets by titanium addition, *J. Rare Earths.* (2022), <https://doi.org/10.1016/j.jre.2022.04.002>.
- [40] C.G. Pope, X-ray diffraction and the Bragg equation, *J. Chem. Educ.* 74 (1997) 129, <https://doi.org/10.1021/ed074p129>.
- [41] M. Çelebi, A. Çanakçı, O. Güler, B. Akgül, A.H. Karabacak, Study on effect of milling time on the mechanical and wear properties of the ZA40-B4C-graphene hybrid nanocomposites fabricated by vacuum hot-pressing, *JOM* 75 (2023) 3935–3950, <https://doi.org/10.1007/s11837-023-06007-x>.
- [42] M. Çelebi, A. Çanakçı, O. Güler, H. Karabacak, B. Akgül, S. Özkaya, A study on the improvement of wear and corrosion properties of ZA40/Graphene/B4C hybrid nanocomposites, *J. Alloy. Compd.* 966 (2023) 171628, <https://doi.org/10.1016/j.jallcom.2023.171628>.
- [43] A.L. Ortiz, L. Shaw, X-ray diffraction analysis of a severely plastically deformed aluminum alloy, *Acta Mater.* 52 (2004) 2185–2197, <https://doi.org/10.1016/j.actamat.2004.01.012>.
- [44] B. Himabindu, N.S.M.P. Latha Devi, B. Rajini Kanth, Microstructural parameters from X-ray peak profile analysis by Williamson-Hall models; A review, *Mater. Today Proc.* 47 (2021) 4891–4896, <https://doi.org/10.1016/j.matpr.2021.06.256>.
- [45] D. Alloyeau, W. Dachraoui, Y. Javed, H. Belkahla, G. Wang, H. Lecoq, S. Ammar, O. Ersen, A. Wisnet, F. Gazeau, C. Ricolleau, Unravelling kinetic and thermodynamic effects on the growth of gold nanoplates by liquid transmission electron microscopy, *Nano Lett.* 15 (2015) 2574–2581, <https://doi.org/10.1021/acs.nanolett.5b00140>.
- [46] Y.-N. Wen, J.-M. Zhang, Surface energy calculation of the fcc metals by using the MAEAM, *Solid State Commun.* 144 (2007) 163–167, <https://doi.org/10.1016/j.ssc.2007.07.012>.
- [47] B. Fu, W. Liu, Z. Li, Calculation of the surface energy of fcc-metals with the empirical electron surface model, *Appl. Surf. Sci.* 256 (2010) 6899–6907, <https://doi.org/10.1016/j.apsusc.2010.04.108>.
- [48] S.J. Park, S.-H. Jo, S. Oh, Y.-S. Oh, S.-J. Kim, H.W. Lee, S.-H. Kang, Y. Hoon Moon, J. Jung, Microstructure-dependent etching behavior of a partially recrystallized Invar alloy, *Mater. Des.* 217 (2022) 110631, <https://doi.org/10.1016/j.matedes.2022.110631>.
- [49] M. Zhang, A.F. Gourges-Lorenzon, E.P. Busso, H. Luo, M. Huang, Recrystallisation-assisted creep of an austenitic Fe-Ni alloy under low stresses after hot deformation, *Acta Mater.* 153 (2018) 23–34, <https://doi.org/10.1016/j.actamat.2018.04.050>.
- [50] P. Opěla, P. Kawulok, I. Schindler, R. Kawulok, S. Rusz, H. Navrátil, On the Zener–Hollomon parameter, multi-layer perceptron and multivariate polynomials in the struggle for the peak and steady-state description, *Metals* 10 (2020) 1413, <https://doi.org/10.3390/met1011413>.
- [51] K. Sato, M. Ichinose, Y. Hirotsu, Y. Inoue, Effects of deformation induced phase transformation and twinning on the mechanical properties of austenitic Fe-Mn-Al alloys, *ISIJ Int.* 29 (1989) 868–877, <https://doi.org/10.2355/isijinternational.29.868>.
- [52] F-06 ASTM, Standard Specification for Iron-Nickel and Iron-Nickel-Cobalt Alloys for Low Thermal Expansion Applications, West Conshohocken, 2016. (<https://doi.org/10.1520/F1684-06R16>).
- [53] X. Shen, S. Liu, X. Wang, C. Cui, P. Gong, L. Zhao, X. Han, Z. Li, Effect of cooling rate on the microstructure evolution and mechanical properties of iron-rich Al-Si alloy, *Materials* 15 (2022) 411, <https://doi.org/10.3390/ma15020411>.
- [54] J. Zhu, L. Zhong, Y. Xu, X. Cai, F. Bai, Y. Ding, Z. Lu, H. Wu, Characterization and formation mechanisms of the TiC-Fe cermet layer in Ti-TiC-Fe composites, *Vacuum* 155 (2018) 631–636, <https://doi.org/10.1016/j.vacuum.2018.06.065>.
- [55] J.M.A. Beattie, J.P. Goss, M.J. Rayson, P.R. Briddon, Electron-affinity and surface-stability of aluminium-oxide terminated diamond surfaces, *Diam. Relat. Mater.* 94 (2019) 137–145, <https://doi.org/10.1016/j.diamond.2019.02.009>.
- [56] M. Çelebi, O. Güler, A. Çanakçı, H. Çuvalcı, The effect of nanoparticle content on the microstructure and mechanical properties of ZA27-Al 2 O 3 -Gr hybrid nanocomposites produced by powder metallurgy, *J. Compos. Mater.* 55 (2021) 3395–3408, <https://doi.org/10.1177/00219983211015719>.
- [57] V.A. Drebushchak, Thermal expansion of solids: review on theories, *J. Therm. Anal. Calorim.* 142 (2020) 1097–1113, <https://doi.org/10.1007/s10973-020-09370-y>.
- [58] V.M. Nadutov, D.L. Vashchuk, A.N. Pilipenko, O.A. Davidenko, Internal friction in Invar Fe-35% Ni alloy after combined SPD by hydroextrusion and drawing, *Funct. Mater.* 21 (2014) 52–58, <https://doi.org/10.15407/fm21.01.052>.
- [59] V.M. Nadutov, D.L. Vashchuk, Y.O. Svystunov, V.A. Beloshenko, V.Z. Spuskanuk, A.A. Davidenko, Magnetic and invar properties of Fe-35%Ni alloy after grinding of structure by hydroextrusion, *Funct. Mater.* 19 (2012) 334–342, <http://dspace.nbu.gov.ua/handle/123456789/135311> (accessed June 1, 2022).
- [60] V.M. Nadutov, S.G. Kosintsev, E.O. Svystunov, O.I. Zaporozhets, Interatomic interaction and magnetostriction in invar FeNi-C-based alloys, *Metallofiz. i Noveishie Tekhnologii* 31 (2009) 1021–1034.
- [61] E. Balikci, A. Raman, R.A. Mirshams, Microstructure and texture effect on the thermal expansion of a variously aged polycrystalline superalloy IN738LC, *Metall. Mater. Trans. A.* 30 (1999) 2803–2808, <https://doi.org/10.1007/s11661-999-0117-6>.
- [62] L.N. Hansen, M.E. Zimmerman, D.L. Kohlstedt, Grain boundary sliding in San Carlos olivine: Flow law parameters and crystallographic-preferred orientation, *J. Geophys. Res.* 116 (2011) B08201, <https://doi.org/10.1029/2011JB008220>.
- [63] F. Erden, B. Akgül, I. Danaci, M.R. Oner, Thermoelectric and thermomechanical properties of invar 36: comparison with common thermoelectric materials, *J. Alloy. Compd.* 932 (2023) 167690, <https://doi.org/10.1016/j.jallcom.2022.167690>.
- [64] T. Sakai, A. Belyakov, R. Kaibyshev, H. Miura, J.J. Jonas, Dynamic and post-dynamic recrystallization under hot, cold and severe plastic deformation conditions, *Prog. Mater. Sci.* 60 (2014) 130–207, <https://doi.org/10.1016/j.pmatsci.2013.09.002>.

- [65] B.-W. Li, Y. Shen, Z.-X. Yue, C.-W. Nan, Enhanced microwave absorption in nickel/hexagonal-ferrite/polymer composites, *Appl. Phys. Lett.* 89 (2006), <https://doi.org/10.1063/1.2357565>.
- [66] M. Müller, H. Harada, H. Warlimont, Magnetic materials, in: Springer Handbooks, Springer, Cham, 2018, pp. 753–807, https://doi.org/10.1007/978-3-319-69743-7_22.
- [67] J. Liu, M.-S. Cao, Q. Luo, H.-L. Shi, W.-Z. Wang, J. Yuan, Electromagnetic property and tunable microwave absorption of 3D nets from nickel chains at elevated temperature, *ACS Appl. Mater. Interfaces* 8 (2016) 22615–22622, <https://doi.org/10.1021/acsami.6b05480>.